The Aeronautical Journal (2024), 1–18
doi:10.1017/aer.2024.47

ROYAL
AERONAUTICAL
SOCIETY

RESEARCH ARTICLE

Numerical investigation of thermochemical non-equilibrium effects in Mach 10 scramjet nozzle

J.P. Wang, C.F. Zhuo, C.L. Dai and B. Sun

School of Mechanical and Engineering, Nanjing University of Science and Technology, Nanjing 210094, China
Corresponding author: C.F. Zhuo; Email: njust203zcf@126.com

Received: 25 October 2023; **Revised:** 15 April 2024; **Accepted:** 17 April 2024

Keywords: hydrocarbon fuel; Mach 10 scramjet nozzle; thermochemical non-equilibrium gas; high temperature; nozzle performance

Abstract

High-temperature non-equilibrium effects are prominent in scramjet nozzle flows at high Mach numbers. Hence, the thermochemical non-equilibrium gas model incorporating the vibrational relaxation process of molecules in the hydrocarbon-air reaction is developed to numerically simulate the flow of a hydrocarbon fuel scramjet nozzle at Mach 10. Besides, the results computed by the models of the thermally perfect gas, chemically non-equilibrium gas, and thermally non-equilibrium chemically frozen gas are applied for comparative studies. Results indicate that chemical non-equilibrium effects are more significant for the flow-field structure and parameters compared to thermal non-equilibrium effects. Meanwhile, vibrational relaxation and chemical reactions interact in the flow-field. The heat released from the chemical reactions in the flow-field of the thermochemical non-equilibrium gas model makes the thermal non-equilibrium effects weaker compared to the thermally non-equilibrium chemically frozen gas model; the chemical reactions in the thermochemical non-equilibrium gas model are more intense than in the chemically non-equilibrium gas model. Due to the slow relaxation of vibrational energy, the thermal non-equilibrium models predicted nozzle thrust lower than the thermal equilibrium models by approximately 1.11% to 1.33%; when considering the chemical reactions, the chemical non-equilibrium models predicted nozzle thrust higher than the chemical frozen models by approximately 7.30% to 7.54%. Hence, the structural design and performance study of the high Mach numbers scramjet nozzle must consider thermochemical non-equilibrium effects.

Nomenclature

t	time (s)
ρ	density (kg/m^3)
D	molar diffusion coefficient (m^2/s)
$\dot{\omega}$	mass generation rate of component (kg/m^3·s)
y	mole fraction
u	velocity (m/s)
P	static pressure (Pa)
E	energy (J/kg)
τ	stress tensor
q	heat flux (W/m^2)
H	enthalpy (J/kg)
N_{m}	number of molecular species
T	static temperature (K)
f	friction (N)
A	preexponential factor ([cm^3/mol]$^{n\text{-}1}$/s)
β	temperature index
F_x	thrust (N)

F_y	lift (N)
M	pitching moment (N·m)

Subscripts

s	species
i,j	direction
v	vibrational
k	reaction order
∞	free stream

Abbreviation

TPG	thermally perfect gas
CNEG	chemically non-equilibrium gas
TNCFG	thermally non-equilibrium chemically frozen gas
TCNEG	thermochemical non-equilibrium gas
TVD	total variation diminishing
QCT	quasi-classical trajectory

1.0 Introduction

As one of the most advanced propulsion systems of hypersonic vehicles, scramjet has become the focus of aerospace research [1–4]. In the operating environment of high Mach numbers, the gas inside the scramjet nozzle is still continuously combusting, and the high temperature generated excites the vibrational energy of the molecules, so the internal flow of the scramjet nozzle is a typical thermochemical non-equilibrium flow process. The different modes of energy excitation and transfer of the gas and the chemical reactions involved in the components affect the energy distribution within the flow-field, significantly changing the aerodynamic thermal environment near the wall; thermochemical non-equilibrium effects also cause changes in the flow-field characteristics, thus affecting the propulsive performance of the nozzle [5].

Recently, the thermochemical non-equilibrium flow features of the high Mach numbers scramjet have been focused on. For example, Dai et al. [6, 7] compared the flow-field features of inward-turning inlet and two-dimensional inlet under thermal non-equilibrium and thermal equilibrium, respectively, and remarked that thermochemical non-equilibrium effects aggravated molecule dissociation. Zuo et al. [8] analysed the impact of wall parameters on non-equilibrium flows at the inlet and found that thermochemical non-equilibrium effects were significant under adiabatic wall conditions. Fiévet et al. [9] found that the pseudoshock structure in the isolator was significantly different from the thermal equilibrium state when thermal non-equilibrium was considered. Ao et al. [10] investigated the flame structure, mixing, and combustion efficiency within a scramjet at different vibration temperatures, and showed that an increase in the vibration temperature of the inflow hinders mixing with the fuel, but higher temperatures promote the dissociation reaction rate and shorten the ignition distance. Shi et al. [11] verified the accuracy of the vibration-chemistry-vibration coupling model in the numerical simulation of detonation cell size through experiments. Voelkel et al. [12] used a quasi-classical trajectory (QCT) approach to modify the reaction rate of conventional two-temperature models and investigate the influence of thermal non-equilibrium on reaction rate during hydrogen-air combustion, pointed out that the use of a detailed reaction mechanism can help to establish a non-equilibrium model. Koo et al. [13] used direct numerical simulation for the flow inside the scramjet combustion chamber under thermochemical non-equilibrium effects and found that ignition delays occurred at vibration temperature lower than the static temperature, which negatively affected the combustion stability. Thus, the study of thermochemical non-equilibrium effects is indispensable for high Mach numbers flows.

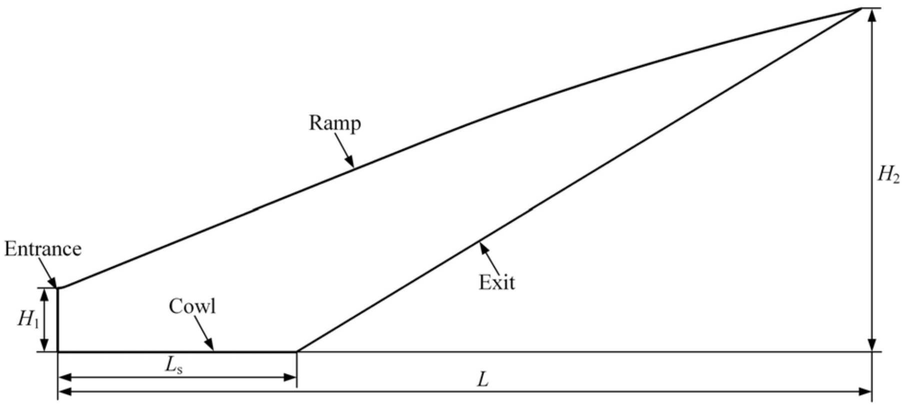

Figure 1. *Geometric configuration of the SERN.*

The nozzle, as the exhaust component of the scramjet, expands the high-enthalpy gas components with obvious non-uniform characteristics flowing from the combustor, which affects the total downstream flow-field and non-equilibrium effects become more significant. However, most relevant studies are focused on the nozzle of high-enthalpy shock tunnel [14–16], which all use Park's two-temperature and air component reaction model for nonequilibrium calculation due to the simplicity of the gas components in the shock tunnel. Sagnier et al. [17] assumed that the airflow remained in a non-equilibrium state only downstream of the nozzle throat, investigated the influence of the vibration-dissociation coupling model on the flow, and the numerical simulation results compared well with the experimental results. Zeitoun et al. [18] analysed thermochemical non-equilibrium effects in conical and contoured nozzles, and the results showed that the flow-field parameters were influenced by the shape of the nozzle divergent part. Teixeira et al. [19] conducted an experimental verification of the impact of the catalytic wall on flow parameters and found that the expansion ratio of the nozzle had a significant influence on the flow parameters at fully catalytic and non-catalytic, except the frozen vibrational-electronic temperature. In addition, there are reports about gas non-equilibrium effects in the nozzle. Zidane et al. [20] used vibrational relaxation times from Skrebkov's theoretical model to better simulate thermochemical non-equilibrium effects in the H_2-O_2 rocket nozzle flow-field, and the results showed that both thermal and chemical non-equilibrium have certain effects on the flow parameters. Whereas, there are few studies on comparative analysis of thermochemical non-equilibrium effects on the performance of hydrocarbon fuel scramjet nozzles.

In this study, thermochemical non-equilibrium effects of hydrocarbon fuel scramjet nozzles at Mach number 10 are investigated by numerical simulation. The flow-field characteristics, wall parameters and performance of the nozzle are predicted by using thermally perfect gas (TPG), chemically non-equilibrium gas (CNEG), thermally non-equilibrium chemically frozen gas (TNCFG) and thermochemical non-equilibrium gas (TCNEG), which provides a reference for performance optimisation and design of high Mach numbers propulsion system.

2.0 Nozzle model and calculation method

2.1 Nozzle model

In this study, a single expansion ramp nozzle (SERN) model based on the maximum thrust theory design is selected for the design conditions of flight altitude 36 km and flight Mach number 10 [21]. The geometric configuration of the SERN is shown in Fig. 1, and the geometric parameters are as follows: entrance height $H_1 = 0.12$ m, lower wall length $L_s = 3.71H_1$, total length $L = 12.5H_1$, and exit height $H_2 = 5.36H_1$.

2.2 Governing equations

In this study, the multi-component compressible Navier-Stokes equations are adopted to simulate high Mach numbers flow. For the thermal equilibrium models (TPG and CNEG), a uniform temperature is used to represent the various states of the molecular internal energy. The conservation equations of mass, momentum and energy can be expressed as follows:

$$\frac{\partial \rho_s}{\partial t} + \frac{\partial \rho_s u_i}{\partial x_i} = \frac{\partial}{\partial x_i}\left(\rho D_s \frac{\partial y_s}{\partial x_i}\right) + \dot{\omega}_s \tag{1}$$

$$\frac{\partial \rho u_i}{\partial t} + \frac{\partial \rho u_i u_j}{\partial x_j} = -\frac{\partial P}{\partial x_i} + \frac{\partial \tau_{ij}}{\partial x_j} \tag{2}$$

$$\frac{\partial \rho E}{\partial t} + \frac{\partial \rho H u_i}{\partial x_i} = \frac{\partial \tau_{ij} u_j}{\partial x_i} + \frac{\partial q_i}{\partial x_i} \tag{3}$$

Where t is the time term; s represents a certain component; i and j represent the direction; ρ_s, D_s, y_s and $\dot{\omega}_s$ are the density, diffusion coefficient, molar fraction, and mass generation rate of component s, respectively; ρ is the density of the mixture; u_i and u_j are the velocity components; P is the static pressure; τ_{ij} is the stress tensor; E and H are the total energy and total enthalpy of the mixture, respectively; q_i is the heat flux component.

In this study, the maximum static temperatures do not exceed 5000 K, so the ionisation of the gas components is not considered in the calculation. When thermal non-equilibrium is considered, the translational and rotational energies of molecules are considered to be in thermal equilibrium and the vibrational energy is considered to be in non-equilibrium [20], Park used the two-temperature model to accurately predict the main characteristics of this non-equilibrium flow [22]. Hence, Park's two-temperature model [23] was applied for calculating the thermal non-equilibrium models (TCNEG and TNCFG) in this study. This model uses the translational-rotational temperature to represent the translational and rotational energy of the molecule, and the vibrational temperature to represent the molecular vibrational energy. When describing the vibrational energy state, this energy conservation equation is shown as follows:

$$\frac{\partial(\rho e_v)}{\partial t} + \frac{\partial(\rho e_v u_i)}{\partial x_i} = \frac{\partial}{\partial x_i}\left(q_{v,i} + \sum_{s=1}^{N_m} \rho D_s e_{v,s} \frac{\partial y_s}{\partial x_i}\right) + \omega_v \tag{4}$$

Where e_v is the vibrational energy of the mixture; $q_{v,i}$ is the vibrational heat flux component; N_m is the number of molecular species; $e_{v,s}$ is the vibrational energy of component s; ω_v is the vibrational energy term of the mixture.

The total energy conservation equation for the thermal non-equilibrium state is:

$$\frac{\partial(\rho E)}{\partial t} + \frac{\partial(\rho H u_i)}{\partial x_i} = \frac{\partial}{\partial x_i}\left(\tau_{ij} u_i + q_{tr,i} + q_{v,i} + \sum_{s=1}^{N_s} \rho H_s D_s \frac{\partial y_s}{\partial x_i}\right) \tag{5}$$

Where $q_{tr,i}$ is the translational-rotational heat flux component; N_s and H_s are the total number and enthalpy of component s, respectively.

2.3 Turbulence model

The Reynolds average Navier-Stokes (RANS) method was used to calculate the flow-field of the nozzle based on its higher numerical simulation efficiency and better prediction ability of complex turbulence. The two-equations realisable k-ε turbulence model [24], which is better for predicting hypersonic flows near the wall of the nozzle, can accurately capture the flow characteristics within the boundary layer and is suitable for predicting non-equilibrium flows in the nozzle. The transport equations for turbulence

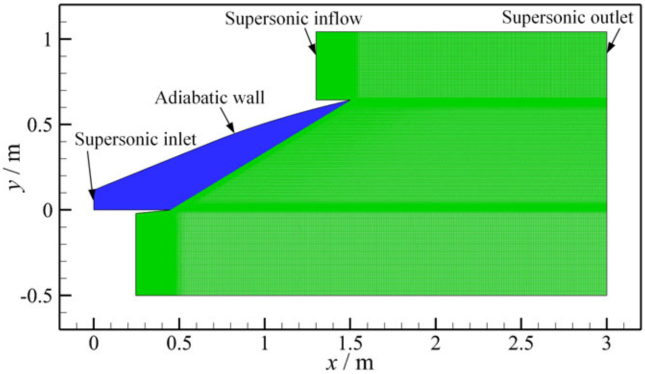

Figure 2. *Computational mesh and boundary conditions.*

kinetic energy k and its rate of dissipation ε for this model are as follows:

$$\frac{\partial(\rho k)}{\partial t}+\frac{\partial(\rho k u_i)}{\partial x_i}=\frac{\partial}{\partial x_j}\left[\left(\mu+\frac{\mu_t}{\sigma_k}\right)\frac{\partial k}{\partial x_j}\right]+P_k-\rho\varepsilon \tag{6}$$

$$\frac{\partial(\rho\varepsilon)}{\partial t}+\frac{\partial(\rho\varepsilon u_i)}{\partial x_i}=\frac{\partial}{\partial x_j}\left[\left(\mu+\frac{\mu_t}{\sigma_\varepsilon}\right)\frac{\partial k}{\partial x_j}\right]+\rho C_1 E\varepsilon-\rho C_2\frac{\varepsilon^2}{k+\sqrt{v\varepsilon}} \tag{7}$$

Where μ_t is the turbulence viscosity; σ_k and P_k are the turbulent Prandtl number and the production of k, respectively; σ_ε is the turbulence Prandtl number of ε; C_1 and C_2 are constants 1.44 and 1.92, respectively.

2.4 Numerical algorithm

In this study, the CFD code [6] is used to numerically simulate the high Mach number flow in the nozzle. The finite volume method is used to solve the governing equations. Polynomial interpolation is performed using the second-order total variation declining (TVD) scheme [25]. The thermodynamic parameters are approximated by polynomial curve fitting [26]. The molecular viscosity is determined using Sutherland's law. The diffusion coefficient is determined by a Schmidt number. The rigidity problem caused by the thermochemical non-equilibrium source term is solved by the second-order point implicit scheme [27]. The multigrid method and variable Courant number are applied to improve the convergence. The results are considered to have reached convergence when the residuals all dropped below 1×10^{-4}.

The calculation domain of the nozzle using structured grids is shown in Fig. 2. Set the mesh size of the first layer close to the wall to 10 μm to ensure that $y^+<10$, the total number of meshes is about 0.2 million. The walls use adiabatic non-slip boundary conditions. The far-field is set to the altitude of 36km and the environmental parameters are as follows: Mach number $M_\infty = 10.0$, static pressure $P_\infty = 498.5$ Pa, static temperature $T_\infty = 239.0$ K, angle of attack $\alpha = 0°$, mass fraction of oxygen $m_{O_2} = 0.23$ and mass fraction of nitrogen $m_{N_2} = 0.77$. The entire flow-field is initialised using pressure far-field conditions. Entrance parameters of the nozzle are as follows: Mach number $M = 2.1$, static temperature $T = 2687.0$ K, static pressure $P = 62374.5$ Pa and entrance components content are shown in Table 1.

2.5 Chemical reaction kinetic model

An eight-component hydrocarbon fuel model is used, containing components CO, CO_2, O_2, H_2, H_2O, OH, H, and O. As shown in Table 2, the 12-step elementary reaction of hydrocarbon fuel is selected in this study, where M is the third collision body; A_j, j, β_j and E_j represent the preexponential factor,

Table 1. *Component content of nozzle entrance*

Specie	Mass fraction
H	1.0×10^{-3}
H_2	1.8×10^{-3}
H_2O	6.0×10^{-2}
OH	1.6×10^{-2}
O	1.0×10^{-3}
O_2	4.5×10^{-2}
CO	8.0×10^{-2}
CO_2	7.5×10^{-2}
N_2	0.7202

Table 2. *Chemical reaction mechanism [28]*

Reaction	$A_j([\mathrm{cm}^3/\mathrm{mol}]^{n-1}/\mathrm{s})$	β_j	E_j(kJ/mol)
$H+O_2 \Longleftrightarrow OH+O$	1.2×10^{17}	−0.91	69.1
$H_2+O \Longleftrightarrow OH+H$	1.5×10^{7}	2.0	31.6
$O+H_2O \Longleftrightarrow OH+OH$	1.5×10^{10}	1.14	72.2
$OH+H_2 \Longleftrightarrow H_2O+H$	1.0×10^{8}	1.6	13.8
$H+O+M \Longleftrightarrow OH+M$	1.0×10^{16}	0.0	0.0
$O+O+M \Longleftrightarrow O_2+M$	1.0×10^{17}	−1.0	0.0
$H+H+M \Longleftrightarrow H_2+M$	9.7×10^{16}	−0.6	0.0
$H_2O+M \Longleftrightarrow OH+H+M$	1.6×10^{17}	0.0	478.0
$H_2+O_2 \Longleftrightarrow OH+OH$	7.94×10^{14}	0.0	187.0
$CO+OH \Longleftrightarrow H+CO_2$	4.4×10^{6}	1.5	−3.1
$CO+O+M \Longleftrightarrow CO_2+M$	5.3×10^{13}	0.0	−19.0
$CO+O_2 \Longleftrightarrow O+CO_2$	2.5×10^{12}	0.0	200.0

Third-body efficiencies for all reactions are 2 for $M = H_2$, 6.0 for H_2O, and 1.0 for all other M.

reaction order, temperature index and reaction activation energy, respectively. The above parameters can be used to calculate the chemical reaction rate k_j by Arrhenius formula:

$$k_j = A_j T^{\beta_j} \exp\left(-\frac{E_j}{R_0 T}\right) \tag{8}$$

Park's two-temperature model states that the chemical reaction rate is determined by the reaction control temperature $T_c = T^n {T_v}^{1-n}$, where T is the translational-rotational temperature; T_v is the vibrational temperature; n is 0.5 for the dissociation reactions and n is 1 for other reactions [23].

In this study, four gas models in Table 3 were selected to analyse the influence of thermal and chemical non-equilibrium effects on flow-field parameters. (1) The TCNEG model includes the vibrational relaxation process and chemical reactions of molecules. (2) The TNCFG model, which assumes that the gas is in a chemically frozen state, only considers the vibrational relaxation process of molecules. (3) Assuming that the vibration relaxation time is very small, the model is regarded as the CNEG model. (4) Set the chemical reaction rate of the CNEG model to be very low to become the TPG model.

2.6 Numerical validation

In this study, the CFD code coupled with the TCNEG model and the k-ε model is employed for simulating the high-temperature flow inside the SERN [29], and the above numerical means have been used to

Table 3. Main features of four thermochemical gas models

Item	Thermochemical non-equilibrium gas (TCNEG)	Thermally non-equilibrium chemically frozen gas (TNCFG)	Chemically non-equilibrium gas (CNEG)	Thermally perfect gas (TPG)
Vibrational relaxation	Non-equilibrium	Non-equilibrium	Equilibrium	Equilibrium
Chemical reaction	Non-equilibrium	Frozen	Non-equilibrium	Frozen

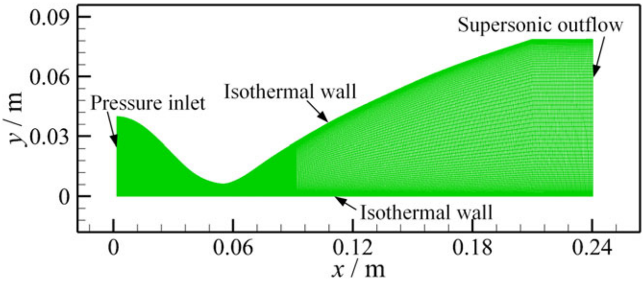

Figure 3. *Computational mesh and boundary conditions of validation SERN.*

predict the thermochemical non-equilibrium flow inside a Mach 12 inward-turning inlet [6]. The grids of the nozzle entrance and wall are encrypted to be able to satisfy the requirements of the turbulence model for y^+ and to ensure the accuracy of the turbulent boundary layer and shock wave calculation results. The computational mesh and boundary conditions of SERN are shown in Fig. 3, the entrance parameters are as follows: total pressure $P_t = 1.1$ MPa, total temperature $T_t = 2{,}376$ K, and entrance components content are shown in Table 4. The wall boundary conditions are isothermal walls where $T_w = 500$ K. Figure 4 indicates that the wall static pressure and exit static and vibrational temperatures obtained through numerical simulation have better agreement with the experimental results. Hence, it is feasible to use this simulation method to predict non-equilibrium flows.

2.7 Grid independence validation

Under the TCNEG model, this study evaluates three different grid distributions of SERN designed in Section 2.1. The grid convergence index is set to 1.1, and the number of the coarse grid, medium grid and refined grid are 0.1 million, 0.2 million and 0.3 million, respectively. From Fig. 5 and Table 5, it can be seen that the wall parameters obtained from the numerical results of the medium and refined grid are essentially the same, while the gap between the coarse and refined grid is relatively large. Thus, the medium grid is selected for the calculation to meet the calculation accuracy and improve efficiency.

3.0 Results and discussion

3.1 Analysis of flow-field characteristics

Figure 6 shows the Mach number contours predicted by different thermochemical models. The high enthalpy gas expands rapidly after entering the nozzle, and significant expansion waves are observed at the entrance and exit of the ramp and cowl, this situation is attributed to the outward deflection of the supersonic gas flow at these locations. Since the pressure at the jet boundary is less than that in the mainstream region, it leads to the phenomenon of inward deflection of the expansion waves at the exit of the ramp and cowl, and these two inwardly deflected expansion waves gradually intersect near

Table 4. *Component content of validation SERN entrance [30]*

Specie	Mass fraction
H_2	0.598×10^{-3}
H	0.154×10^{-4}
O_2	0.266×10^{-2}
O	0.692×10^{-4}
H_2O	0.248
OH	0.219×10^{-2}
N	0.128×10^{-7}
NO	0.212×10^{-2}
N_2	0.744

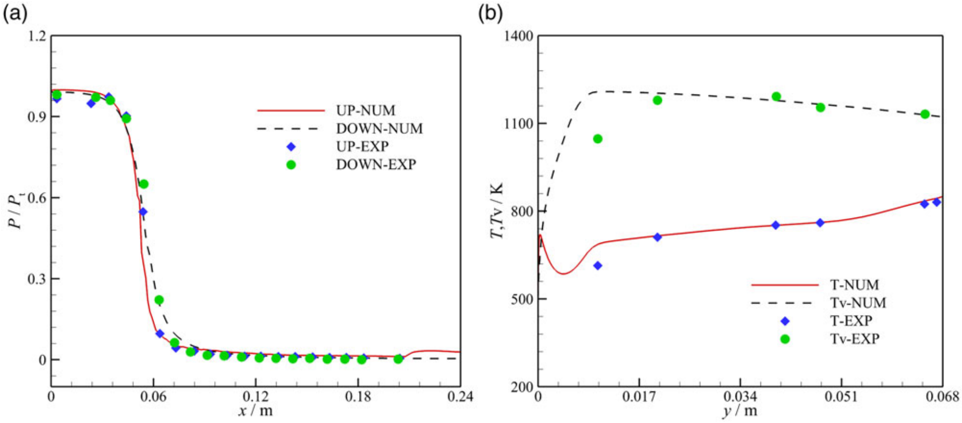

Figure 4. *Comparison of (a) wall static pressure and (b) exit static and vibrational temperature.*

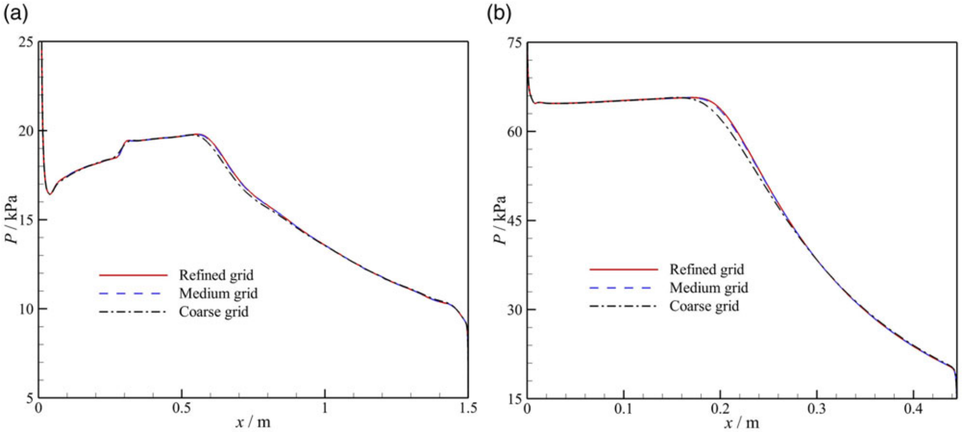

Figure 5. *Comparison of the (a) ramp and (b) cowl static pressure.*

Table 5. *Maximum gap between different grid distributions and refined grid*

Item	Ramp	Cowl
Refined grid	0	0
Medium grid	0.22%	0.47%
Coarse grid	1.33%	2.88%

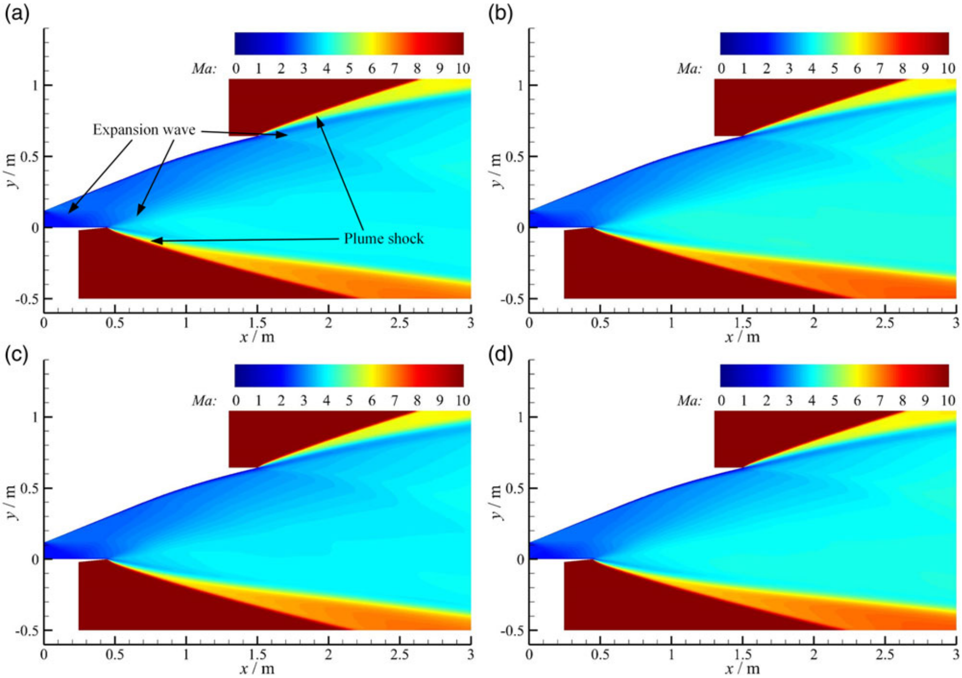

Figure 6. *Mach number contours of the (a) TCNEG, (b) TNCFG, (c) CNEG and (d) TPG.*

the exit of the nozzle as the flow develops rapidly. The contact of the expanding gas flow with the supersonic free stream produces an attached oblique surge, called the plume shock. There also exists a plume mixing layer between the plume shock and the gas flow, where the chemical non-equilibrium models (TCNEG and CNEG) secondary combustion, and the thickness of the re-ignition zone is gradually widened with the flow, which provides more chemical energy to the flow-field, therefore effectively improves the propulsive performance of the scramjet to a certain extent. From Fig. 6, compared with the TCNEG model, the CNEG model has a slightly lower degree of nozzle internal expansion and exit Mach number; the TNCFG model has a significantly higher degree of nozzle internal expansion and downstream Mach number than the TCNEG model, which indicate that chemical non-equilibrium effects are more significant for the flow-field structure and parameters compared to thermal non-equilibrium effects.

Figure 7 shows the static temperature contours of different gas models. After the gas enters the nozzle, there is also continued combustion of components and recombination reactions of molecules, and this process releases more chemical energy and heat for the flow-field, so the static temperature of the flow-field in the chemical non-equilibrium models is significantly higher than that in the chemical frozen models (TNCFG and TPG). In the thermal equilibrium models, more vibrational energy needs to be transferred to the translational-rotational energy to reach the thermal equilibrium state, which leads to

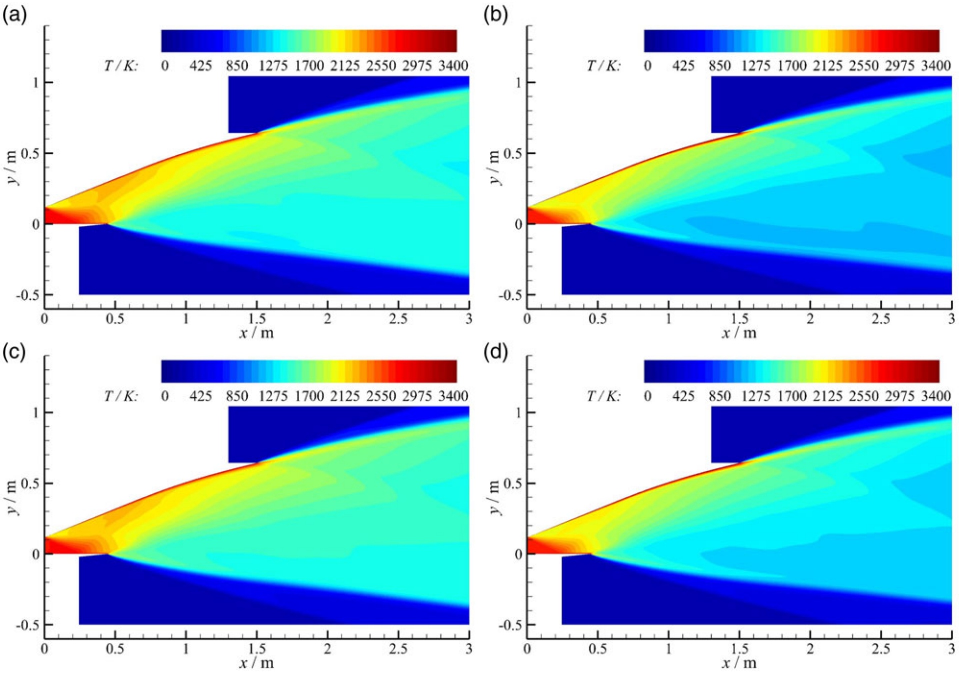

Figure 7. *Static temperature contours of the (a) TCNEG, (b) TNCFG, (c) CNEG and (d) TPG.*

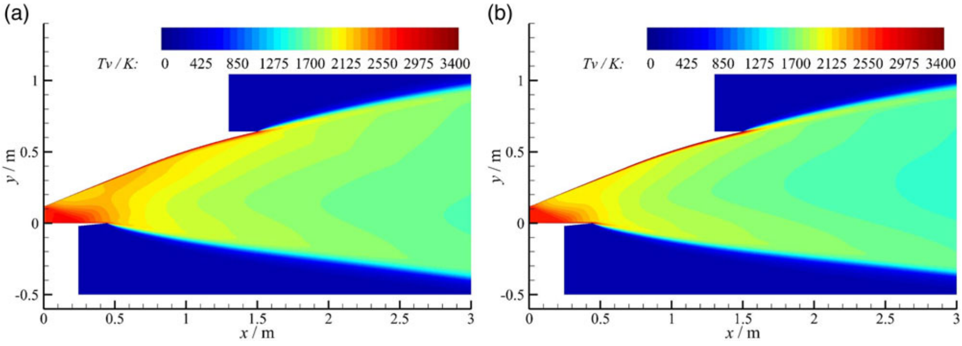

Figure 8. *Vibrational temperature contours of the (a) TCNEG and (b) TNCFG.*

lower translational-rotational energy in the thermal non-equilibrium models than in the thermal equilibrium models, which means that the static temperature of the flow-field in the thermal non-equilibrium models is relatively low. Meanwhile, the static temperature of the boundary layer is higher than that of the mainstream region under the effect of viscous stagnation, while the static temperature of the chemical non-equilibrium models is lower than the chemical frozen models in this region due to the endothermic effects of dissociation reactions.

Figure 8 shows the vibrational temperature contours of the thermal non-equilibrium models. The static temperature near the entrance and wall is higher, leading to the complete excitation of vibrational energy, so the vibrational temperature is higher in this region. The vibrational temperature of the TCNEG model is relatively higher in the mainstream region since its static temperature is higher here compared to the TNCFG model. Due to the slow vibrational relaxation, the trend of vibrational temperature in the flow-field is relatively delayed compared with the static temperature.

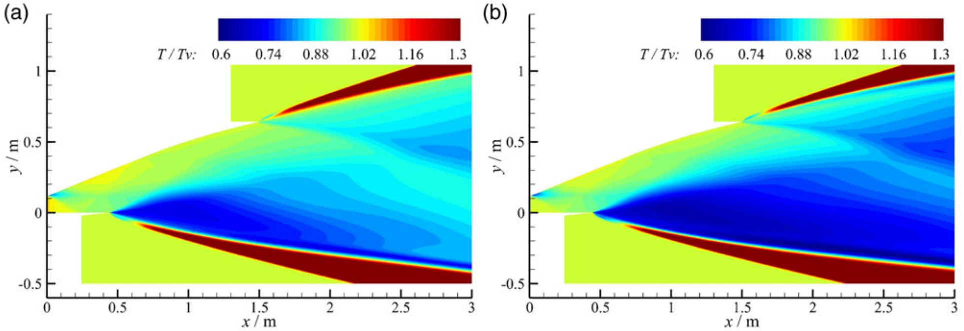

Figure 9. *Ratio of* T *to* $\mathrm{T_v}$ *of the (a) TCNEG and (b) TNCFG.*

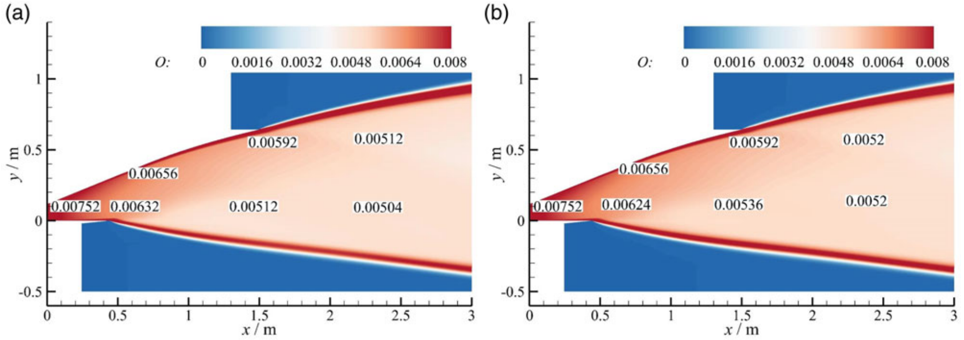

Figure 10. *Oxygen atom distributions of the (a) TCNEG and (b) CNEG.*

3.2 Analysis of non-equilibrium effects

This study has adopted the ratio of the static temperature to the vibrational temperature to represent thermal non-equilibrium effects in the flow-field. From Fig. 10, in the TNCFG model, the high temperature near the nozzle entrance and boundary layer causes fully excited vibrational energy, so the flow-field is close to thermal equilibrium here. Since the relaxation time of the vibrational energy is much longer than the translational-rotational energy, the vibrational temperature decreases slower than the static temperature under the expansion wave at the entrance of the ramp, and the static temperature rises faster than the vibrational temperature under the plume shock at the exit of the ramp and cowl. Downstream of the exit, the rapid decrease in static temperature suppresses vibrational relaxation, resulting in the strongest thermal non-equilibrium effects here. The difference in the degree of thermal non-equilibrium between the TCNEG and TNCFG model downstream of the nozzle exit is mainly attributed to the influence of heat release from the incomplete reaction gas in the TCNEG model on the static and vibrational temperature.

Figure 10 shows the distributions of oxygen atoms for the chemical non-equilibrium models. Oxygen atoms come from the chemical reactions of components. In the TCNEG model, it can be observed that the oxygen atoms are primarily found in the nozzle entrance and boundary layer, where the higher vibrational temperature promotes the oxygen dissociation reaction; at the mainstream region, the dissociation reaction ability is weakened and the recombination reaction of oxygen atoms is significant, so the oxygen atoms content decreases rapidly with the flow. Compared with the CNEG model, the TCNEG model has a slightly lower content of oxygen atoms downstream of the exit, which implies that the recombination reaction capacity of the oxygen atoms will be enhanced under longer vibrational relaxation times.

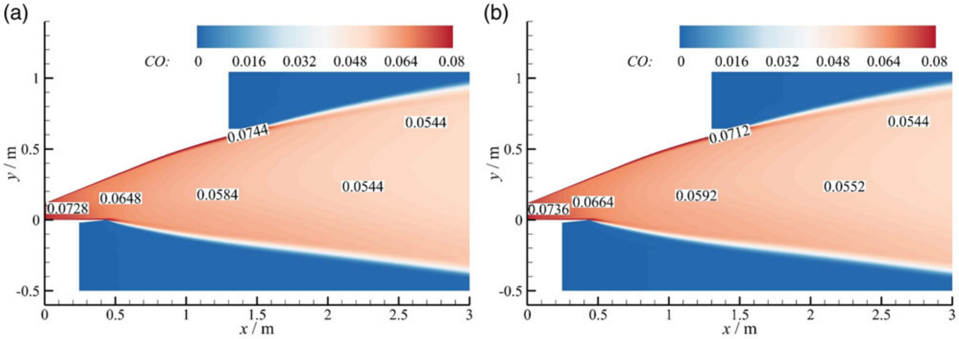

__Figure 11.__ Carbon monoxide distributions of the (a) TCNEG and (b) CNEG.

Figure 11 shows the carbon monoxide distributions of the chemical non-equilibrium models. Carbon monoxide is produced from the chemical reactions of carbon dioxide, its content is higher in the nozzle entrance and boundary layer. At the mainstream region, the lower carbon monoxide content of the TCNEG model compared to the CNEG model has two main influences: the dissociation reaction is affected by vibrational relaxation, and the recombination reaction is more intense in the TCNEG model.

3.3 Analysis of mainstream parameters

This study analyses the flow variations in the mainstream region of the nozzle using parameter distributions on the center streamline. Since the position of the nozzle exit, the difference in Mach number between the different models gradually increases, the Mach number of the chemical frozen models is significantly higher than the chemical non-equilibrium models. Static pressure difference at the nozzle exit becomes obvious, the static pressure of the TCNEG model is lower than the CNEG model and higher than the TNCFG model, which is caused by the influence of the slow vibrational energy relaxation and chemical reactions, respectively.

As highlighted in Fig. 12(c), the heat released from the combustion reactions of components at the nozzle entrance causes the vibrational temperature to rise as well. The static temperature of all models decreases rapidly with flow under the influence of the expansion wave and the static temperature of the thermal non-equilibrium models drops significantly faster than the vibrational temperature, which exhibits the phenomenon of excessive vibrational excitation, and the thermal non-equilibrium phenomenon becomes more and more obvious with the flow. From Fig. 12(d), the chemical non-equilibrium models consume a large amount of oxygen for the combustion reactions at the entrance, while downstream of the exit, the TCNEG model enhances the recombination reaction capacity resulting in a slightly higher oxygen content than the CNEG model. In Fig. 12(e) and (f), it can be seen that the TCNEG model chemical reactions are more intense than the CNEG model.

3.4 Analysis of wall parameters

Figure 13 illustrates the various parameter distributions at the ramp. The static pressure on the ramp decreases rapidly at the entrance and after $x = 0.6$ m under the effect of the expansion wave. While at the rest of the ramp, the wall pressure of the chemically non-equilibrium gas models gradually increases by chemical reactions, the chemical frozen gas models have little change for static pressure. At $x = 0.3$ m, there is a weak oblique shock from the cowl entrance, so the static pressure tends to increase for all four models. On the whole, the chemical non-equilibrium models have higher static pressure than the chemical frozen models. The chemical non-equilibrium models have a lower static temperature than the

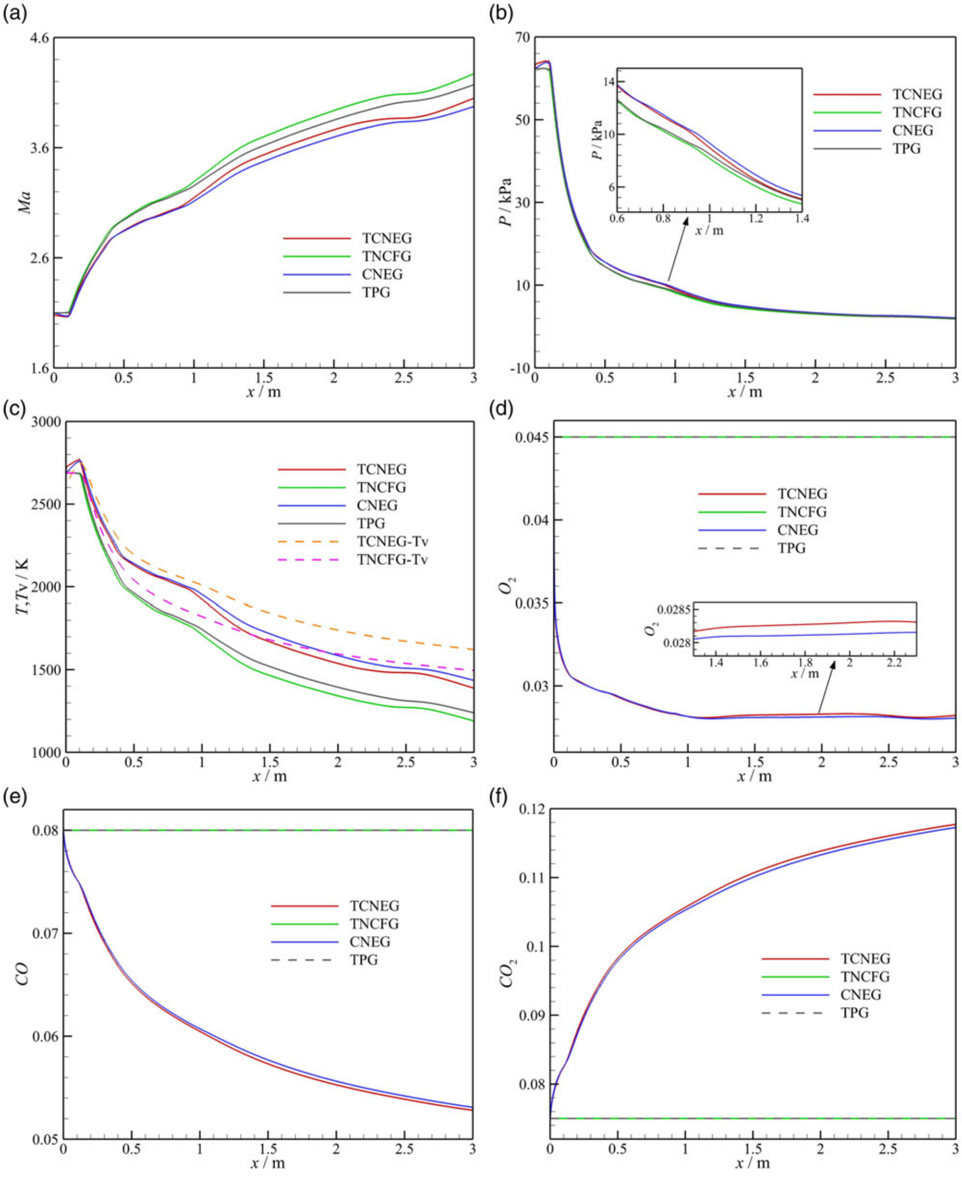

Figure 12. *Distribution of (a) Mach number, (b) static pressure, (c) static and vibrational temperature, (d) oxygen mass fraction, (e) carbon monoxide mass fraction and (f) carbon dioxide mass fraction on the center streamline for different gas models.*

chemical frozen models under the dissociation reaction. The reduced transfer of energy between the different models in thermal non-equilibrium causes the static temperature of the TNCFG and TCNEG models to be higher than the TPG and CNEG models, respectively. Compared with the TNCFG model, the vibrational temperature of the TCNEG model near the boundary layer is lower, which implies that some of the vibrational energies are being consumed by dissociation reactions in this region.

The fully excited vibrational energy on the ramp leads to the intense dissociation reactions of components, and the content of carbon monoxide and hydrogen is constantly increasing. The TCNEG model shows a decreasing and then increasing trend in the hydrogen mass fraction near the entrance, which

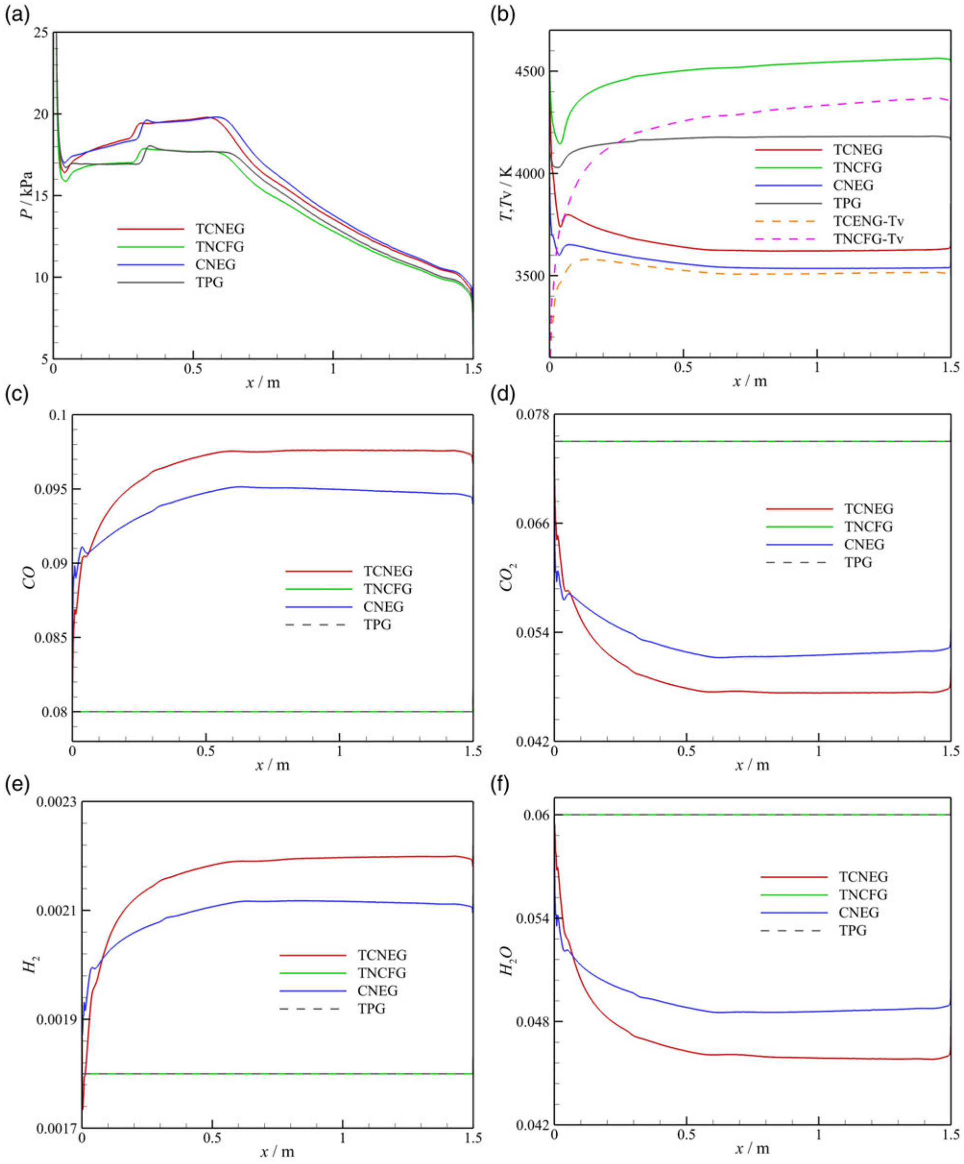

Figure 13. *Distribution of (a) static pressure, (b) static and vibrational temperature, (c) carbon monoxide mass fraction, (d) carbon dioxide mass fraction, (e) hydrogen mass fraction and (f) water mass fraction at the ramp.*

is a part of the mass consumed by combustion reactions here. The mass fraction of carbon dioxide and water shows a decreasing trend near the entrance of the ramp, which indicates that chemical reactions are very intense here, and the mass fraction of components changes very little after the development to $x = 0.6$ m.

Figure 14 illustrates the various parameter distributions at the cowl. Consistent with the static pressure and static temperature distributions on the ramp, the static pressure of the CNEG and TCNEG models is greater than the TPG and TNCFG models, and the static temperature of the TNCFG and TPG models is higher than the TCNEG and CNEG models, but the static pressure and static temperature are numerically higher than the parameters of the ramp, which is mainly due to the nozzle structure affects the flow-field

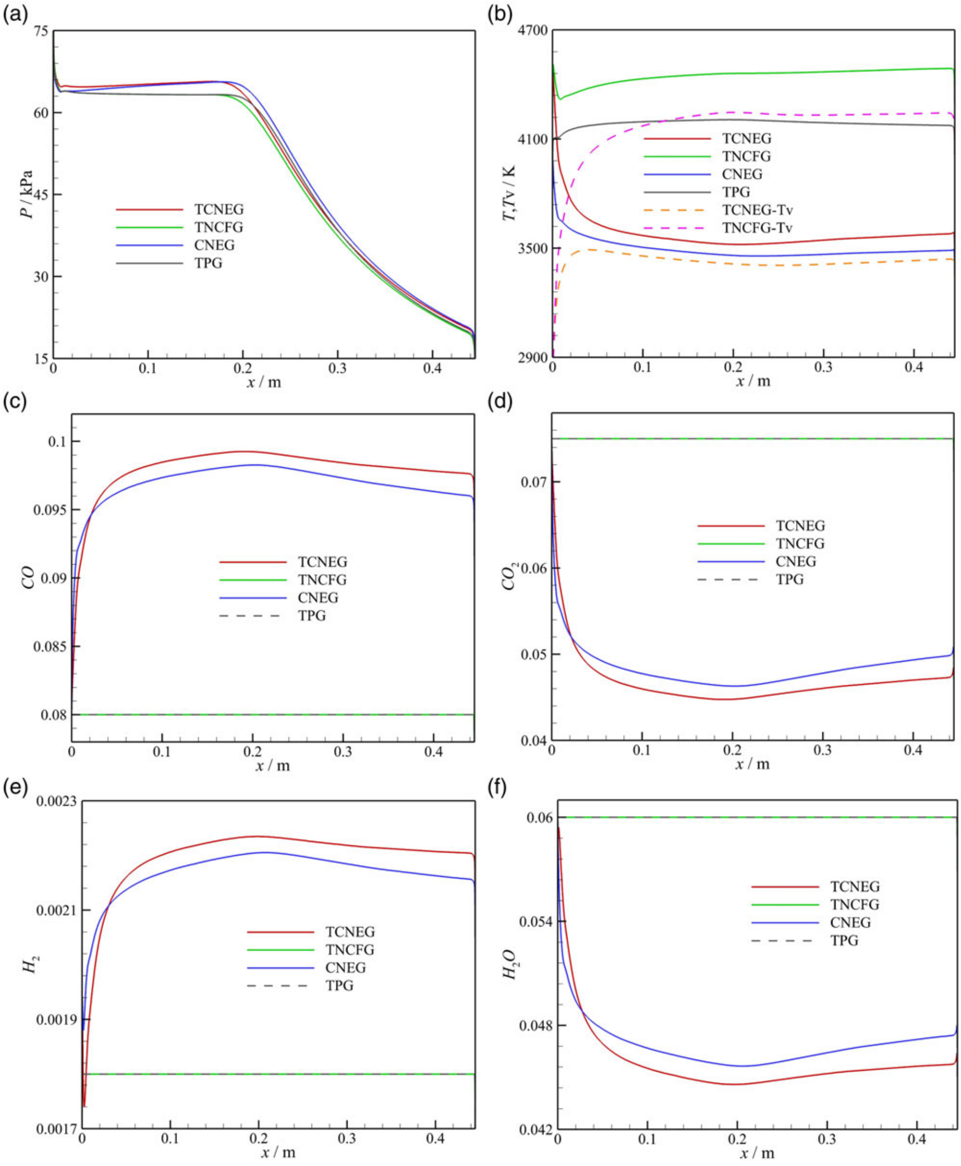

Figure 14. *Distribution of (a) static pressure, (b) static and vibrational temperature, (c) carbon monoxide mass fraction, (d) carbon dioxide mass fraction, (e) hydrogen mass fraction and (f) water mass fraction at the cowl.*

here. In terms of the mass fraction of components, chemical reactions on the cowl are more intense relative to the ramp. After $x = 0.22$ m, the expansion wave at the entrance is reflected on the cowl, which causes the static pressure to decrease rapidly and the chemical reaction activity to be affected.

3.5 Analysis of nozzle performance

Table 6 illustrates the nozzle performance parameters for different gas models at Mach number 10, where F_x, F_y and M represent the thrust, lift and pitching moment, respectively. The pitching moment

Table 6. *Performance parameters of nozzle*

Model	F_x/N	F_y/N	M/(N·m)
TCNEG	7572.22	1149.29	13925.41
TNCFG	7041.46	157.73	12839.69
CNEG	7656.98	1215.41	14126.08
TPG	7136.23	245.51	13066.06

origin is selected as the intersection of the entrance and the cowl. Compared with the TCNEG model, the TNCFG model does not consider the continuous combustion of gas in the nozzle, the dissociation and recombination reactions of the components, and ignores the influence of chemical reactions on the wall pressure, so its performance parameters are significantly lower. The CNEG model uses the one-temperature model and does not consider the effect of vibrational energy freezing on the wall pressure, so its performance parameters are higher than the TCNEG model. Since chemical non-equilibrium effects have a greater influence on the flow-field than thermal non-equilibrium effects, the performance parameters of the TCNEG model considering both chemical reactions and vibrational relaxation is higher than the TPG model.

4.0 Concusions

This study accomplished the simulation of nozzle flow with Mach 10 at 36 km with TPG, CNEG, TNCFG and TCNEG models. The influence of thermochemical non-equilibrium effects on the flow-field characteristics, wall parameters and working performance of the nozzle are analysed. The main results are given as follows:

(1) The chemical frozen models have large expansion inside the nozzle and higher Mach numbers at the exit compared to the chemical non-equilibrium models. Chemical non-equilibrium effects are more significant for the flow-field structure and parameters compared to thermal non-equilibrium effects.

(2) The nozzle entrance and around the wall are close to thermal equilibrium. In the mainstream region, thermal non-equilibrium effects are gradually significant with flows. Compared with the TNCFG model, the heat released by chemical reactions in the TCNEG model flow-field makes the non-equilibrium effects weaker.

(3) At the mainstream region, chemical reactions are most intense inside the nozzle. The dissociation reaction capacity of the nozzle boundary layer is more intense than the mainstream region. Overall, the TCNEG model has more intense chemical reactions than the CNEG model in the flow-field.

(4) For the nozzle performances, the thermal non-equilibrium models predicted nozzle thrust lower than the thermal equilibrium models by approximately 1.11% to 1.33%, and the chemical non-equilibrium models predicted nozzle thrust higher than the chemical frozen models by approximately 7.30% to 7.54%.

Acknowledgements. The authors express sincere gratitude to the support of the National Natural Science Foundation of China (No. 11602109), China Scholarship Council (No. 202206840048), Training Fund for Excellent Doctoral Candidates of Nanjing University of Science and Technology, XXX National Key Laboratory Fund (No. 2022-XXXX-LB-020-01), and Key laboratory of hypersonic aerodynamic force and heat technology, AVIC Aerodynamics Research Institute (No. XFX20220104).

Competing interest. The authors declare that they have no known competing financial interests or personal relationships that could have appeared to influence the work reported in this paper.

References

[1] Curran E.T. Scramjet engines: the first forty years. *J. Propul. Power*, 2001, **17**, (6), pp 1138–1148. doi: 10.2514/2.5875

[2] Laurence S.J., Schramm J.M., Karl S. and Hannemann K. An experimental investigation of steady and unsteady combustion phenomena in the HyShot II combustor. In *17th AIAA International Space Planes and Hypersonic Systems and Technologies Conferences*, AIAA Paper, 2011. doi: 10.2514/6.2011-2310

[3] Karl S. and Hannemann K. CFD Analysis of the HyShot II scramjet experiments in the HEG shock tunnel. In *15th AIAA International Space Planes and Hypersonic Systems and Technologies Conferences*, AIAA Paper, 2008. doi: 10.2514/6.2008-2548

[4] Kindler M., Lempke M., Blacha T., Gerlinger P. and Aigner M. Numerical investigation of the HyShot supersonic combustion configuration. In *44th AIAA/ASME/SAE/ASEE Joint Propulsion Conference and Exhibit*, AIAA Paper, 2008. doi: 10.2514/6.2008-5167

[5] Kumar S., Pandey K.M. and Sharma K.K. Recent developments in technological innovations in scramjet engines: a review. *Mater. Today Proc.*, 2021, **45**, pp 6874–6881. doi: 10.1016/j.matpr.2020.12.1086

[6] Dai C.L., Sun B., Zhou C.S., Zhuo C.F., Du L. and Zhou S.B. Numerical investigation of real-gas effect of inward-turning inlet at Mach 12. *Aerosp. Sci. Technol.*, 2021, **115**, p 106786. doi: 10.1016/j.ast.2021.106786

[7] Dai C.L., Sun B., Zhou S.B., Zhuo C.F., Zhou C.S. and Yue L.J. Influence of high temperature non-equilibrium effects on Mach 12 scramjet inlet. *Acta Astronaut.*, 2022, **193**, pp 237–254. doi: 10.1016/j.actaastro.2022.01.013

[8] Zuo F.Y., Mölder S. and Hu S.L. Thermochemical non-equilibrium effects on hypersonic wavecatcher intake at Mach 12. *Acta Astronaut.*, 2022, **198**, pp 56–68. doi: 10.1016/j.actaastro.2022.05.030

[9] Fiévet R. and Raman V. Effect of vibrational nonequilibrium on isolator shock structure. *J. Propul. Power.*, 2018, **34**, (5), pp 1334–1344. doi: 10.2514/1.B37108

[10] Ao Y., Wu K., Lu H.B., Ji F. and Fan X.J. Combustion dynamics of high Mach number scramjet under different inflow thermal nonequilibrium conditions. *Acta Astronaut.*, 2023, **208**, pp 281–295. doi: 10.1016/j.actaastro.2023.04.020

[11] Shi L.S., Shen H., Zhang P., Zhang D.L. and Wen C. Assessment of vibrational non-equilibrium effect on detonation cell size. *Combust. Sci. Technol.*, 2017, **189**, (5), pp 841–853. doi: 10.1080/00102202.2016.1260561

[12] Voelkel S., Raman V. and Varghese P.L. Effect of thermal nonequilibrium on reactions in hydrogen combustion. *Shock Waves*, 2016, **26**, pp 539–549. doi: 10.1007/s00193-016-0645-0

[13] Koo H., Raman V. and Varghese P.L. Direct numerical simulation of supersonic combustion with thermal nonequilibrium. *Proc. Combust. Inst.*, 2015, **35**, (2), pp 2145–2153. doi: 10.1016/j.proci.2014.08.005

[14] Kaneko M., Men'Shov I. and Nakamura Y. Computation of nozzle starting process with thermal and chemical nonequilibrium in high-enthalpy shock tunnel. In *40th AIAA Aerospace Sciences Meeting and Exhibit*, AIAA Paper, 2002. doi: 10.2514/6.2002-142

[15] Schramm J.M., Karl S., Hannemann K. and Steelant J. Ground testing of the HyShot II scramjet configuration in HEG. In *15th AIAA International Space Planes and Hypersonic Systems and Technologies Conference*, AIAA Paper, 2008. doi: 10.2514/6.2008-2547

[16] Kaneko M., Men'Shov I. and Nakamura Y. Numerical simulation of nonequilibrium flow in high-enthalpy shock tunnel with EIH scheme. In *15th AIAA Computational Fluid Dynamics Conference*, AIAA Paper, 2001. doi: 10.2514/6.2001-2860

[17] Sagnier P. and Marraffa L. Parametric study of thermal and chemical nonequilibrium nozzle flow, *AIAA J.*, 1991, **29**, (3), pp 334–343. doi: 10.2514/3.59921

[18] Zeitoun D., Boccaccio E., Druguet M.C. and Imbert M. Reactive and viscous flow in hypersonic nozzles. AIAA J. 1994, 32, (2), pp 333–340. doi: 10.2514/3.11989

[19] Teixeira O. and Páscoa J. "Catalytic wall effects for hypersonic nozzle flow in thermochemical non-equilibrium. *Acta Astronaut.*, 2023, **203**, pp 48–59. doi: 10.1016/j.actaastro.2022.11.031

[20] Zidane A., Haoui R., Sellam M. and Bouyahiaoui Z. Numerical study of a nonequilibrium H2−O2 rocket nozzle flow. *Int. J. Hydrogen Energy*, 2019, **44**, pp 4361–4373. doi: 10.1016/j.ijhydene.2018.12.149

[21] Yu K.K., Chen Y.L., Huang S. and Xu J.L. Inverse design method on scramjet nozzles based on maximum thrust theory. *Acta Astronaut.*, 2020, **166**, pp 162–171. doi: 10.1016/j.actaastro.2019.10.024

[22] Park C. Assessment of a two-temperature kinetic model for dissociating and weakly ionizing nitrogen. *J. Thermophys. Heat Transf.*, 1988, **2**, (1), pp 8–16. doi: 10.2514.3/55

[23] Park C. Assessment of two-temperature kinetic model for ionizing air. *J. Thermophys. Heat Transf.*, 1989, **3**, (3), pp 233–244. https://arc.aiaa.org/doi/10.2514/3.28771

[24] Goldberg U., Peroomian O. and Chakravarthy S. A wall-distance-free k-ε model with enhanced near-wall treatment. *J. Fluids Eng.*, 1998, **120**, pp 457–462. doi: 10.1115/1.2820684

[25] Harten A. High-resolution schemes for hyperbolic conservation laws. *J. Comput. Phys.*, 1983, **49**, (3), pp 357–393. doi: 10.1016/0021-9991(83)90136-5

[26] Gupta R.N., Yos J.M. and Thompson R.A. A review of reaction rates and thermodynamic and transport properties for the 11-species air model for chemical and thermal nonequilibrium calculations to 30000 K, Technical Report No. NASA/TP1990-1323.

[27] Edwards J.R. A diagonal implicit/nonlinear multigrid algorithm for computing hypersonic, chemically-reacting viscous flows. In *32nd Aerospace Sciences Meeting and Exhibit*, AIAA Paper, 1994. doi: 10.2514/6.1994-762

[28] Nietubicz C. and Gibeling H. Navier-Stokes computations for a reacting, M864 base bleed projectile. In *31st Aerospace Sciences Meeting*, American Institute of Aeronautics and Astronautics, 1993. doi: 10.2514/6.1993-504

[29] Weisgerber H., Fischer M., Magens E., Winandy A., Foerster W. and Beversdorff M. Experimental analysis of the flow of exhaust gas in a hypersonic nozzle. In *8th AIAA International Space Planes and Hypersonic Systems and Technologies Conference*, AIAA Paper, 1998. doi: 10.2514/6.1998-1600

[30] Link T. and Koschel W.W. Computation of a nonequilibrium expansion flow in a single expansion ramp nozzle. *J. Propul. Power.*, 2001, **17**, (6), pp 1353–1360. doi: 10.2514/2.5887

Cite this article: Wang J.P., Zhuo C.F., Dai C.L. and Sun B. Numerical investigation of thermochemical non-equilibrium effects in Mach 10 scramjet nozzle. *The Aeronautical Journal*, https://doi.org/10.1017/aer.2024.47